Microstructure-Guided Constitutive Modeling and Fracture Prediction of Cementitious Systems

Sumanta Das[1], Narayanan Neithalath[2]

Abstract

This paper presents a microstructure-guided numerical modeling approach to predict the effective constitutive response and the fracture properties of cementitious materials. Prediction of the effective constitutive response for cement mortar involves generation of virtual microstructure consisting of cement paste matrix, sand particles and interfacial transition zone. The generated virtual microstructure is meshed and periodic boundary conditions are implemented in order to represent displacement and traction continuity across repetitive unit cells. A uniaxial strain is then applied on the RVE and the analysis is implemented through conventional FE solver. Thus this approach simulates a strain- (or displacement) controlled test scenario. To efficiently handle post-processing of the simulated element stresses/strains, a homogenization module is developed to obtain effective constitutive response of the material. The constitutive behavior, predicted through the microstructure-based approach correlates very well with experimental measurements for cement mortar. The homogenized constitutive response for cement mortar is used in a damage model to predict fracture properties of cement mortar using extended finite element analysis. The damage model incorporates a maximum principal stress based damage initiation criteria and a bilinear traction-separation law is used for damage evolution. The current damage model accurately predicts the fracture properties for cement mortar. The validation of the methodology presented here provides confidence on its ability to be applied for many novel sustainable binders as well as binders with modified inclusions towards microstructure-guided design of such systems.

1. Assistant Research Professor, School of Sustainable Engineering and the Built Environment, Arizona State University, Tempe, AZ 85287 (email:Sumanta.Das@asu.edu).
2. Associate Professor, School of Sustainable Engineering and the Built Environment, Arizona State University, Tempe, AZ 85287 (email: Narayanan.Neithalath@asu.edu).

I. INTRODUCTION

The link between the material microstructure and relevant mechanical behavior provides valuable information towards design and development of sustainable cementitious materials for several applications. In recent years, many novel cementitious composites have emerged, consisting of cement-free binders [1–3] as well as incorporating several types of inclusion materials for various special applications such as the use of lightweight aggregates (LWAs) for internal curing, reduction of dead load, thermal and acoustic insulation [4–7], microencapsulated phase change materials (PCM) for control of thermal cracking in pavements and bridge decks [8], and regulating internal environment in buildings [9,10], waste and recycled materials such as rubber for energy absorption [11], and denser/stiffer aggregates for radiation shielding [12,13]. Incorporation of such inclusions or modification in the binder phase influences the individual stresses in the microstructural components and the stress distributions in the composite, thereby dictating the failure path/mechanism of the material. Traditionally trial and error-based experimental testing is being used for property-evaluation as well as design of such new materials without looking into the real phenomena occurring at the micro level of the composites that dictate macro-scale behavior. In an attempt to develop a framework for prediction of constitutive behavior and damage in cementitious materials, this study employs a microstructure-guided micromechanical modeling scheme using the finite element method to predict constitutive relationship and applies the obtained information to predict the fracture behavior using extended finite element method (XFEM). Application of the framework on prediction of fracture behavior of cement mortar is elucidated in this paper. However, the modelling framework presented herein is not restricted to cement mortar and can tackle any cementitious systems with binder or inclusion modification. This approach eliminates the shortcomings of the analytical schemes [14–16] and thus yields a better solution. However, the accuracy of predictions depends on the capability to adequately represent the microstructure and appropriate identification of damage parameters especially for non-conventional binder systems. Thus this study intends to demonstrate a numerical approach that can be used in conjunction with reliable microstructural descriptors, thereby enabling adequate prediction of the macroscopic constitutive response and fracture behavior of cementitious materials, which in-turn facilitates microstructure-guided material design.

II. MICROSTRUCTURAL MODEL FOR PREDICTION OF ELASTIC PROPERTY

This section describes the microstructure-guided constitutive modeling framework for cement mortar. The constitutive response of cement mortar, predicted in this section through microstructural stress analysis, is used in the forthcoming section as an input to the homogenized damage model for prediction of fracture property of cement mortar.

A. Elastic Property of Component Phases

The constitutive relationships for all the components: cement paste, quartz aggregates and the paste-inclusion interface are considered in their respective linear elastic regimes only. The default elastic properties of the components, extracted from available literature [17–23], are presented in Table 1.

Table 1. Elastic properties of the components of the mortar for FE simulations

Elastic property	**Component phases**		
	Hardened cement paste	***Quartz inclusion***	***Quartz-cement paste interface***
Young's Modulus, E (GPa)	20	70	15
Poisson's Ratio	0.22	0.17	0.22

B. Numerical Simulation for Elastic Property prediction

This section describes the numerical simulation framework for prediction of constitutive response of cement mortar. The framework explained herein executes microstructure-guided analysis of cement mortar involving generation of a unit cell based on known inclusion size distributions, meshing of the unit cell and application of appropriate boundary conditions, and microstructural stress analysis.

Generation of RVE is accomplished here using Lubachhevsky-Stillinger algorithm [24–27]. The algorithm uses hard contact model and hence particle overlap is not allowed. Here, the RVE is set to be a cube. First, the desired number of particles are randomly distributed inside the periodic bounding box with random initial velocities of the particles. The radius of each particle is initialized at zero. The radius of i^{th} particles in the next event is then increased with different growth rates:

$$\{1\}\ \frac{dr_i}{dt} = g_i$$

Where I = 1, 2,……, number of particles. The growth rate of different particles are controlled so as to attain the desired particle size distribution. The growth rate is computed using finite difference scheme as follows:

$$\{2\}\ g_i = \frac{(r_i^{n+1} - r_i^n)}{\Delta t}$$

The particle radii are updated as follows:

$$\{3\}\ r_i^{n+1} = r_i^n + g_i \Delta t$$

Now, the position of particle 'i' is updated considering a constant velocity between the time nodes:

$$\{4\}\ x_i^{n+1} = x_i^n + v_i^n \Delta t$$

The vector that connects centers of particles 'i' and 'j' is obtained by subtracting position vectors of the two particles:

$$\{5\}\ I_{ij}^{n+1} = x_j^{n+1} - x_i^{n+1}$$

The particles 'i' and 'j' are in contact if the sum of their radii is equal to the length of the connection vector. The time step size can be calculated as:

$$\{6\}\ \Delta t = \min\left[\frac{-V \pm \sqrt{V^2 - UW}}{U}\right]$$

Where $\Delta t > 0$ and V, U and W are given as:

$$\{7a\}\ V = I_{ij}^n.[v_j^n - v_i^n] - [r_i^n + r_j^n][g_i + g_j]$$

$$\{7b\}\ U = [v_j^n - v_i^n]^2 - [g_i + g_j]^2$$

$$\{7c\}\ W = [I_{ij}^n]^2 - [r_i^n + r_j^n]^2$$

This time step calculation (Equation 6) is performed for each particle pair that are being able to collide and thus minimum time step for all the possible collisions is adopted to move forward for the next event. All the particle positions x_i^{n+1} are updated using forward Euler scheme (Equation 4) and new search for next collision is started. The post-contact velocities are computed as follows:

$$\{8a\}\ v_{n_i}^{n+1^+} = \min\{v_{n_i}^{n+1^-}, v_{n_j}^{n+1^-}) - g_i;$$

$$\{8b\}\ v_{n_j}^{n+1^+} = \max\{v_{n_i}^{n+1^-}, v_{n_j}^{n+1^-}) + g_i;$$

Thus, all the above-mentioned steps are repeated and in the process of iterations the particles change position in the bounding box, collide and grow in order to obtain desired volume fraction. Finally, the obtained microstructural information is implemented through a python language script to enable it to be imported to finite element software such as ABAQUS™. After the generation of the microstructure, the REA is meshed using a Python script through ABAQUS™ and thus an orphan mesh file is obtained.

Periodic boundary conditions [28–30] are employed in the 2D REA as shown in Figure 1. Figure 1(a) shows schematic periodic arrays of repetitive unit cells and Figure 1(b) shows the periodic boundary conditions applied on one of such schematic representative elements for illustration. Periodic boundary condition ensures two continuity criteria at the boundaries of neighboring unit cells in order to ensure assembly of individual unit cells as a physical continuous body [31]: (i) displacement continuity, i.e., neighboring unit cells cannot be separated or they cannot penetrate each other; and (ii) traction continuity at the boundary of neighboring unit cells. The displacement field in any periodic microstructure is given as:

$$\{9\}\ v_i(x_1, x_2) = \varepsilon_{ij}^0 x_j + v_i^*(x_1, x_2)$$

Here, ε_{ij}^0 is the applied strain tensor, and v_i^* is a periodic function representing the modification of linear displacement field due to the heterogeneous microstructure. For, the unit cell shown in Figure 1(b), the displacements on a pair of parallel opposite boundary edges are given as:

$$\{10a\}\ v_i^{s+} = \varepsilon_{ij}^0 x_j^{s+} + v_i^*$$

$$\{10b\}\ v_i^{s-} = \varepsilon_{ij}^0 x_j^{s-} + v_i^*$$

Here, s^+ and s^- are s[th] pair of two opposite parallel boundary surfaces of the unit cell as shown in Figure 3(b). The periodic function v^* is the same at both the parallel opposite edges due to periodicity. The difference between the displacement fields of the two opposite parallel boundary edges is given as:

$$\{11\}\ v_i^{s+} - v_i^{s-} = \varepsilon_{ij}^0 (x_j^{s+} - x_j^{s-}) = \varepsilon_{ij}^0 \Delta x_j^s$$

For a pair of opposite parallel boundary edges, Δx_j^s is constant for a specified ε_{ij}^0. Such equations are applied as nodal displacement constraints in the finite element (FE) microstructural analysis.

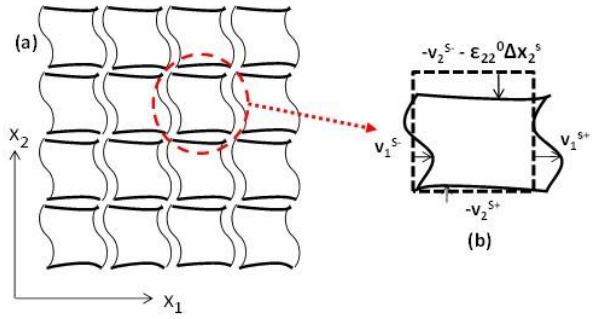

Figure 1: Schematic representative element area (REA) under applied strain (ε_{22}^0) with periodic boundary conditions.

Periodic boundary condition is implemented on the REA as nodal displacement constraints through a Python language program appended to the previously obtained orphan mesh file containing the periodic microstructure information. A specific strain is applied on the REA and the analysis is implemented through ABAQUSTM solver. Thus this approach simulates a strain- (or displacement) controlled test scenario. To efficiently handle post-processing of the simulated individual element stresses, a homogenization module is developed to obtain effective area-averaged REA stresses/strains.

Figure 2(a) shows the generated periodic microstructure and Figure 2(b) shows the stress distribution obtained after analysis under the application of an imposed strain of 0.12% (which is well within the linear elastic range of cementitious systems). This value of strain provided an average REA stress of 36.13 MPa. Free quad-dominated 4-noded bilinear plane strain quadrilateral elements (CPE4R element implemented in ABAQUSTM) are used in the FE models. A mesh convergence study was conducted so as to establish the mesh size for FE analysis. For an REA of 4.15 mm x 4.15 mm, a seed size of 0.0175 mm was found to yield converging responses for all sizes and volume fractions of inclusions. The finest mesh (68879 nodes and 68771 elements) that yielded a converged solution is shown in Figure 2(b). In order to determine the Young's modulus, the microstructural stress analysis is performed for different externally applied strains. The stress-strain response thus generated through numerical

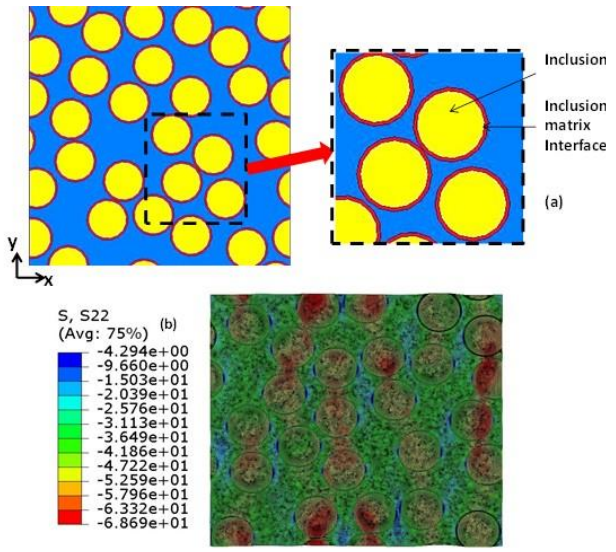

Figure 2: (a) FE model showing the inclusions with the interfacial zones around them. The model contains 50% of inclusions by volume (or area); (b) effect of random distribution and periodic boundary conditions on the stress distribution under an imposed strain of 0.12%. The average REA stress is 36.13 MPa.

simulation is shown in Figure 3 and Young's modulus of 31.4 GPa is obtained. The obtained homogenized Young's modulus correlates well with standard value reported in the literature for cement mortar [22]. The obtained Young's modulus is used in the forthcoming section as input to predict the fracture behavior of homogenized cement mortar.

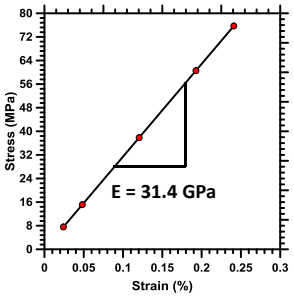

Figure 3: linear constitutive relationship for quartz mortar systems obtained through numerical simulation

III. PREDICTION OF FRACTURE PROPERTIES

This section describes application of extended finite element method (XFEM) to predict damage behavior in cement mortar. The theory and numerical simulation results are shown in the following sub sections:

A. Damage in Cement Mortar

The fracture simulation on notched mortar beams is performed here using extended finite element framework (X-FEM). In the X-FEM framework the local enrichment functions are incorporated in the finite element approximation in order to model the crack (discontinuities) in a relatively efficient manner as compared to the conventional FE. The X-FEM framework ensures the presence of discontinuities through special enriched functions with additional degrees of freedom and simulates path-independent crack initiation and propagation based on damage criteria provided. The approximation of displacement vector function with the partition of unity enrichment is given as:

$$\{12\}\ u = \sum_{I=1}^{N} N_I(x)[u_I + H(x)a_I + \sum_{\alpha=1}^{4} F_\alpha(x) b_I^\alpha]$$

where, $N_I(x)$ are the conventional nodal shape functions; u_I is the nodal displacement vector associated with the continuous part of the finite element solution; a_I is the nodal enriched degree of freedom vector and $H(x)$ is the discontinuous jump across the crack surfaces; b_I^α is the product of nodal enriched degree of freedom vector, $F_\alpha(x)$ are the associated elastic asymptotic crack-tip functions. $H(x)$ is written as:

$\{13\}\ H(x) = 1$ if $(x - x^*).n \geq 0$; otherwise it is equal to -1. where, x is sample Gauss point and x* is the point on the crack closest to x and n is the unit outward normal to the crack at x*. The asymptotic crack tip functions are given as:

$$\{14\}\ F_\alpha(x) = [\sqrt{r}Sin\frac{\theta}{2}, \sqrt{r}Cos\frac{\theta}{2}, \sqrt{r}Sin\theta.Sin\frac{\theta}{2}, \sqrt{r}Sin\theta.Cos\frac{\theta}{2}$$

where, crack tip is at the origin of the polar coordinate system and $\theta = 0$ is the tangent to the crack tip. The damage model also requires appropriate damage initiation criteria. Here, the maximum principal stress criteria is adopted and the crack initiates if the maximum principal stress exceeds the tensile strength of concrete. A bilinear traction separation law [32] has been adopted here for damage propagation. Figure 3 shows the bilinear traction-separation law implemented in the damage model.

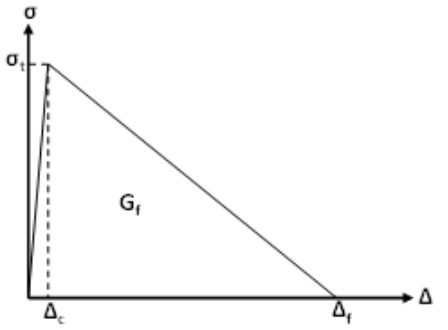

Figure 4: A graphical illustration of the bilinear traction-separation law used to assess concrete damage propagation.

Here σ_t represents the tensile strength of the material, Δ_c is the critical crack tip opening displacement, Δ_f is the separation at failure and G_f is the fracture energy which is the area under the traction-separation curve. The numerical simulation framework also incorporates Concrete damage-plasticity (CDP) model [33,34] beyond the linear elastic regime for fracture simulation. In this model, isotropic damage is represented as:

$$\{15\}\ \sigma = (1-d)D_0^{el} : (\varepsilon - \varepsilon^{pl}) = D^{el} : (\varepsilon - \varepsilon^{pl})$$

where, σ is the Cauchy stress tensor and d is the scalar stiffness degradation variable, ε is the strain tensor, D_0^{el} is the initial elastic stiffness of the material. The effective stress tensor is given as:

$$\{16\}\ \bar{\sigma} = D_0^{el} : (\varepsilon - \varepsilon^{pl})$$

Damage states in tension and compression are characterized independently and plastic flow at the tip of the crack is governed by the flow potential function:

$$\{17\}\ \dot{\varepsilon}^{pl} = \dot{\lambda}\frac{\partial G(\bar{\sigma})}{\partial(\bar{\sigma})}$$

where, the flow potential is given as:

$$\{18\}\ G = \sqrt{(f_c - m.f_t.\tan\beta)^2 + \bar{q}^2} - \bar{p}.\tan\beta - \sigma$$

where, f_t is the tensile strength and f_c is the compressive strength; β is the dilation angle and m is the eccentricity of the plastic potential surface. $\bar{p}$ is the effective hydrostatic stress and $\bar{q}$ is the Mises equivalent effective stress. The CDP model uses a yield condition based on loading function:

$$\{19\}\ F = \frac{1}{1-\alpha}(\bar{q} - 3.\alpha.\bar{p} + \theta(\varepsilon^{pl})\langle\bar{\sigma}_{\max}\rangle - \gamma\langle -\bar{\sigma}_{\max}\rangle) - \bar{\sigma}_c(\varepsilon^{pl})$$

here, the function $\theta(\varepsilon^{pl})$ is given as:

$$\{20\}\ \theta(\varepsilon^{pl}) = \frac{\bar{\sigma}_c(\varepsilon_c^{pl})}{\bar{\sigma}_t(\varepsilon_t^{pl})}(1-\alpha) - (1+\alpha)$$

And, the parameter α is defined as:

$$\{21\}\ \alpha = \frac{(f_{b0}/f_c) - 1}{2(f_{b0}/f_c) - 1}$$

B. Numerical Simulation of Three-point-bending Test for Mortar Beams

The three-point-bending test has been simulated using XFEM. The meshed beam (100 mm (span) x 25 mm (depth) x 25 mm (thickness)) model is shown in Figure 5.

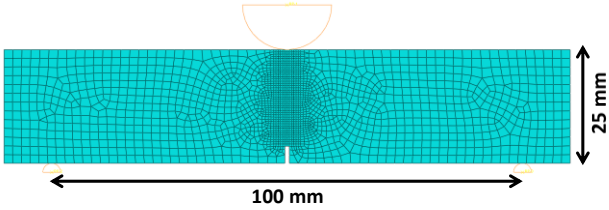

Figure 5: Meshed notched beam for XFEM simulation

The beam has an initial notch (3.75 mm (depth) and 1 mm (width)) at the mid span. Two pin supports at the bottom and the punch at the top are defined as rigid body. The displacement is applied at the reference point tied to the punch. The material parameters for XFEM simulation are shown in Table 2 [22,35,36].

Table 2: material properties for XFEM simulation

E (GPa)	***V***	***Max. Principal stress (MPa)***	G_{f_I} ***(N/mm)***
31.4	0.22	3.0	0.03

Traction-separation behavior has been quantified using data available in the literature [35]. The fracture energy, critical crack tip opening displacement, and tensile strength are used to define the traction-separation behavior [32]. The concrete damage plasticity (CDP) variables (β: dilation angle at high confining pressure, m: eccentricity of the plastic potential surface, γ: parameter that determines the shape of the loading surface in the deviatoric plane and f: the ratio of biaxial compressive strength to uniaxial compressive strength

of concrete) are adopted from the literature [33]. The uniaxial tension and compression behavior of cement mortar for CDP model, adopted from literature [36], are shown in Figure 6.

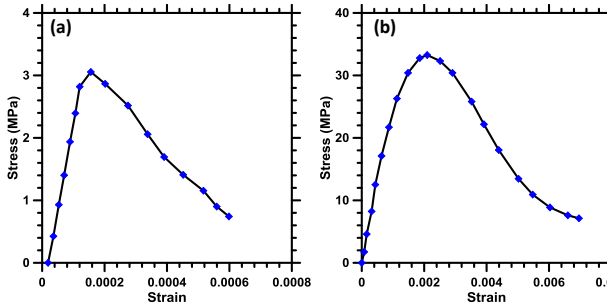

Figure 6: Uniaxial (a) tension and (b) compression behavior implemented within the concrete damage plasticity (CDP model)

Figure 7 shows the generated load-crack mouth opening displacement (CMOD) response obtained through XFEM simulation.

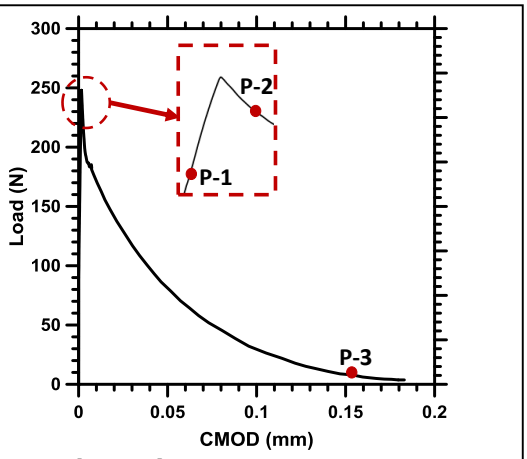

Figure 7: The Load-CMOD response using XFEM

The maximum principal stress contours at three different stages in the load-CMOD response are shown in Figure 8. Point P-1 corresponds to 85% of the peak load in the pre-peak regime whereas point P-2 corresponds to 95% of the peak laod in the post-peak regime. Point P-3 is chosen at a CMOD value of 0.155 mm which is very close to the ultimate failure.Figure 8(a), (b) and (c) exhibit maximum principal stress contours corresponding to points P-1, P-2 and P-3 respectively as shown in Figure 7. Figure 8(a) does not exhibit formation of crack since the maximum principal stress (2.62 MPa) is lower as comapred to the tensile strength (3 MPa) of cement mortar. The crack is observed to be initiated close to the peak load when the maximum principal stress reaches the tensile strength. Figure 8(b) shows the stress contour corresponding to 95% of the peak load in the post peak regime. The crack is visible at this stage and the stress-concentration near the tip of the crack is also visible as expected. Figure 8(c) shows almost complete propagation of the crack near failure.

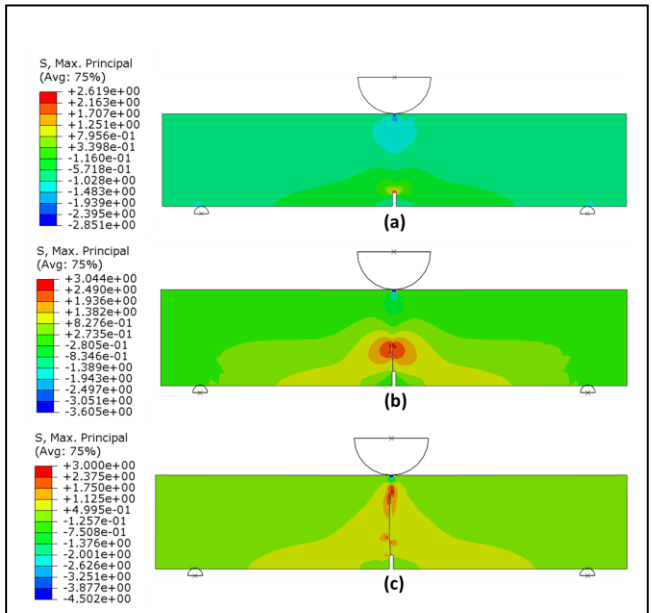

Figure 8: Maximum principal stress contours: (a) P-1(85% of the peak load in pre-peak regime); (b) P-2 (95% of the peak load in post-peak regime) and (c) P-3 (near failure: CMOD: 0.155 mm)

The information on crack extension at 95% of the peak laod in the post-peak regime can be used to calculate the fracture toughness of the cement mortar as follows [37,38]:

{22a} $$K_{IC} = \frac{PL}{bd^{3/2}} F[\frac{a_{eff}}{d}]$$

{22b}

$$F[\frac{a_{eff}}{d}] = [2.9(\frac{a_{eff}}{d})^{1/2} - 4.6(\frac{a_{eff}}{d})^{3/2} + 21.8(\frac{a_{eff}}{d})^{5/2} - 37.6(\frac{a_{eff}}{d})^{7/2} + 38.7(\frac{a_{eff}}{d})^{9/2}]$$

where the effective crack length, $a_{eff} = a_0 + \Delta a$. The $CTOD_c$ value for cement mortar is obtained from XFEM simulation as the CTOD value measured at 95% of the peak load in the post-peak regime (P-2 in Figure 7). The $CTOD_C$ and K_{IC} values, thus calculated using XFEM framework, are reported in Table 2.

Table 2: Comparison of the KIC and CTODc values determined using XFEM and experiment

K_{IC} (MPa.mm$^{0.5}$)		$CTOD_c$ (mm)	
XFEM	Experimental	XFEM	Experimental
27.4	26.4	0.012	0.0125

Table 2 also reports experimentally obtained values adopted from literature [39] for cement mortar. There is a good correlation between the K_{IC} and $CTOD_c$ values obtained from the XFEM framework and the experimental measurements,

establishing the viability of using XFEM framework in determining the fracture properties of cementitious systems.

IV. CONCLUSION

This paper presents a comprehensive numerical approach to predict fracture properties of cementitious systems. The modelling framework presented herein employs microstructure-guided constitutive modelling of cement mortar using conventional finite element analysis and the obtained constitutive relationship for cement mortar is used to predict damage behavior of cement mortar using extended finite element analysis. The fracture properties for cement mortar, thus obtained through numerical simulation, correlates very well with the experimental measurements. The validation of the methodology presented here provides confidence on its ability to be applied for many novel sustainable binders as well as binders with modified inclusions towards microstructure-guided design of such systems which is the ultimate goal of this research work.

REFERENCES

[1] D. Ravikumar, S. Peethamparan, and N. Neithalath, "Structure and strength of NaOH activated concretes containing fly ash or GGBFS as the sole binder," *Cem. Concr. Compos.*, vol. 32, no. 6, pp. 399–410, Jul. 2010.

[2] S. Das, B. Souliman, D. Stone, and N. Neithalath, "Synthesis and Properties of a Novel Structural Binder Utilizing the Chemistry of Iron Carbonation," *ACS Appl. Mater. Interfaces*, vol. 6, no. 11, pp. 8295–8304, Jun. 2014.

[3] M. C. G. Juenger, F. Winnefeld, J. L. Provis, and J. H. Ideker, "Advances in alternative cementitious binders," *Cem. Concr. Res.*, vol. 41, no. 12, pp. 1232–1243, Dec. 2011.

[4] K. S. Al-Jabri, A. W. Hago, A. S. Al-Nuaimi, and A. H. Al-Saidy, "Concrete blocks for thermal insulation in hot climate," *Cem. Concr. Res.*, vol. 35, no. 8, pp. 1472–1479, Aug. 2005.

[5] D. Cusson and T. Hoogeveen, "Internal curing of high-performance concrete with pre-soaked fine lightweight aggregate for prevention of autogenous shrinkage cracking," *Cem. Concr. Res.*, vol. 38, no. 6, pp. 757–765, Jun. 2008.

[6] H. K. Kim, J. H. Jeon, and H. K. Lee, "Workability, and mechanical, acoustic and thermal properties of lightweight aggregate concrete with a high volume of entrained air," *Constr. Build. Mater.*, vol. 29, pp. 193–200, Apr. 2012.

[7] L. H. Nguyen, A.-L. Beaucour, S. Ortola, and A. Noumowé, "Influence of the volume fraction and the nature of fine lightweight aggregates on the thermal and mechanical properties of structural concrete," *Constr. Build. Mater.*, vol. 51, pp. 121–132, Jan. 2014.

[8] F. Fernandes, S. Manari, M. Aguayo, K. Santos, T. Oey, Z. Wei, G. Falzone, N. Neithalath, and G. Sant, "On the feasibility of using phase change materials (PCMs) to mitigate thermal cracking in cementitious materials," *Cem. Concr. Compos.*, vol. 51, pp. 14–26, Aug. 2014.

[9] L. Hembade, N. Neithalath, and S. D. Rajan, "Understanding the energy implications of phase-change materials in concrete walls through finite-element analysis," *J. Energy Eng.*, vol. 140, no. 1, p. 04013009, 2013.

[10] A. M. Thiele, A. Jamet, G. Sant, and L. Pilon, "Annual energy analysis of concrete containing phase change materials for building envelopes," *Energy Convers. Manag.*, vol. 103, pp. 374–386, Oct. 2015.

[11] F. Hernández-Olivares, G. Barluenga, M. Bollati, and B. Witoszek, "Static and dynamic behaviour of recycled tyre rubber-filled concrete," *Cem. Concr. Res.*, vol. 32, no. 10, pp. 1587–1596, Oct. 2002.

[12] I. Akkurt, C. Basyigit, S. Kilincarslan, B. Mavi, and A. Akkurt, "Radiation shielding of concretes containing different aggregates," *Cem. Concr. Compos.*, vol. 28, no. 2, pp. 153–157, Feb. 2006.

[13] A. S. Makarious, I. I. Bashter, A. El-Sayed Abdo, M. Samir Abdel Azim, and W. A. Kansouh, "On the utilization of heavy concrete for radiation shielding," *Ann. Nucl. Energy*, vol. 23, no. 3, pp. 195–206, Feb. 1996.

[14] T. Mori and K. Tanaka, "Average stress in matrix and average elastic energy of materials with misfitting inclusions," *Acta Metall.*, vol. 21, no. 5, pp. 571–574, May 1973.

[15] M. Hori and S. Nemat-Nasser, "Double-inclusion model and overall moduli of multi-phase composites," *Mech. Mater.*, vol. 14, no. 3, pp. 189–206, Jan. 1993.

[16] S. Das, P. Yang, S. S. Singh, J. C. E. Mertens, X. Xiao, N. Chawla, and N. Neithalath, "Effective properties of a fly ash geopolymer: Synergistic application of X-ray synchrotron tomography, nanoindentation, and homogenization models," *Cem. Concr. Res.*, vol. 2015, no. 2015, Sep. 2015.

[17] F. Grondin and M. Matallah, "How to consider the Interfacial Transition Zones in the finite element modelling of concrete?," *Cem. Concr. Res.*, vol. 58, pp. 67–75, Apr. 2014.

[18] Z. Hashin and P. J. M. Monteiro, "An inverse method to determine the elastic properties of the interphase between the aggregate and the cement paste," *Cem. Concr. Res.*, vol. 32, no. 8, pp. 1291–1300, Aug. 2002.

[19] Y. Ke, A. L. Beaucour, S. Ortola, H. Dumontet, and R. Cabrillac, "Influence of volume fraction and characteristics of lightweight aggregates on the mechanical properties of concrete," *Constr. Build. Mater.*, vol. 23, no. 8, pp. 2821–2828, Aug. 2009.

[20] M. P. Lutz, P. J. M. Monteiro, and R. W. Zimmerman, "Inhomogeneous interfacial transition zone model for the bulk modulus of mortar," *Cem. Concr. Res.*, vol. 27, no. 7, pp. 1113–1122, Jul. 1997.

[21] A. U. Nilsen, P. J. M. Monteiro, and O. E. Gjørv, "Estimation of the elastic moduli of lightweight aggregate," *Cem. Concr. Res.*, vol. 25, no. 2, pp. 276–280, Feb. 1995.

[22] C. C. Yang, "Effect of the Transition Zone on the Elastic Moduli of Mortar," *Cem. Concr. Res.*, vol. 28, no. 5, pp. 727–736, May 1998.

[23] V. Zanjani Zadeh and C. P. Bobko, "Nanomechanical characteristics of lightweight aggregate concrete containing supplementary cementitious materials exposed to elevated temperature," *Constr. Build. Mater.*, vol. 51, pp. 198–206, Jan. 2014.

[24] B. D. Lubachevsky and F. H. Stillinger, "Geometric properties of random disk packings," *J. Stat. Phys.*, vol. 60, no. 5–6, pp. 561–583, 1990.

[25] B. D. Lubachevsky, "How to simulate billiards and similar systems," *J. Comput. Phys.*, vol. 94, no. 2, pp. 255–283, 1991.

[26] B. D. Lubachevsky, F. H. Stillinger, and E. N. Pinson, "Disks vs. spheres: Contrasting properties of random packings," *J. Stat. Phys.*, vol. 64, no. 3–4, pp. 501–524, 1991.

[27] H. A. Meier, E. Kuhl, and P. Steinmann, "A note on the generation of periodic granular microstructures based on

grain size distributions," *Int. J. Numer. Anal. Methods Geomech.*, vol. 32, no. 5, p. 509, 2008.
[28] S. Li, "Boundary conditions for unit cells from periodic microstructures and their implications," *Compos. Sci. Technol.*, vol. 68, no. 9, pp. 1962–1974, Jul. 2008.
[29] O. van der Sluis, P. J. G. Schreurs, W. A. M. Brekelmans, and H. E. H. Meijer, "Overall behaviour of heterogeneous elastoviscoplastic materials: effect of microstructural modelling," *Mech. Mater.*, vol. 32, no. 8, pp. 449–462, Aug. 2000.
[30] Z. Xia, C. Zhou, Q. Yong, and X. Wang, "On selection of repeated unit cell model and application of unified periodic boundary conditions in micro-mechanical analysis of composites," *Int. J. Solids Struct.*, vol. 43, no. 2, pp. 266–278, Jan. 2006.
[31] P. Suquet, "Elements of homogenization for inelastic solid mechanics," 1987.
[32] J. Roesler, G. H. Paulino, K. Park, and C. Gaedicke, "Concrete fracture prediction using bilinear softening," *Cem. Concr. Compos.*, vol. 29, no. 4, pp. 300–312, Apr. 2007.
[33] T. Jankowiak and T. Lodygowski, "Identification of parameters of concrete damage plasticity constitutive model," *Found. Civ. Environ. Eng.*, vol. 6, no. 1, pp. 53–69, 2005.
[34] G. Z. Voyiadjis, Z. N. Taqieddin, and P. I. Kattan, "Anisotropic damage–plasticity model for concrete," *Int. J. Plast.*, vol. 24, no. 10, pp. 1946–1965, 2008.
[35] S. Das, M. Aguayo, G. Sant, B. Mobasher, and N. Neithalath, "Fracture process zone and tensile behavior of blended binders containing limestone powder," *Cem. Concr. Res.*, vol. 73, pp. 51–62, Jul. 2015.
[36] S.-M. Kim and R. K. Abu Al-Rub, "Meso-scale computational modeling of the plastic-damage response of cementitious composites," *Cem. Concr. Res.*, vol. 41, no. 3, pp. 339–358, Mar. 2011.
[37] L. C. S. Nunes and J. M. L. Reis, "Estimation of crack-tip-opening displacement and crack extension of glass fiber reinforced polymer mortars using digital image correlation method," *Mater. Des.*, vol. 33, pp. 248–253, Jan. 2012.
[38] E. E. Gdoutos, *Fracture mechanics: an introduction*, vol. 123. Springer, 2006.
[39] S. Das, M. Aguayo, V. Dey, R. Kachala, B. Mobasher, G. Sant, and N. Neithalath, "The fracture response of blended formulations containing limestone powder: Evaluations using two-parameter fracture model and digital image correlation," *Cem. Concr. Compos.*, vol. 53, pp. 316–326, Oct. 2014.